Journal of
Materials Chemistry A

ROYAL SOCIETY
OF CHEMISTRY

PAPER

View Article Online
View Journal | View Issue

Check for updates

Cite this: *J. Mater. Chem. A*, 2020, **8**, 11210

Polyimide/ZIF-7 mixed-matrix membranes: understanding the *in situ* confined formation of the ZIF-7 phases inside a polymer and their effects on gas separations†

Sunghwan Park,‡[a] Kie Yong Cho‡[ab] and Hae-Kwon Jeong *[ac]

Received 9th March 2020
Accepted 5th May 2020

DOI: 10.1039/d0ta02761h

rsc.li/materials-a

Polymer-modification-enabled *in situ* metal–organic framework formation (PMMOF) is potentially a paradigm-shifting preparation method for polymer/MOF mixed-matrix membranes (MMMs). However, the actual reaction conditions of the *in situ* formation of MOFs in a confined polymer free volume are expected to be quite different from that in a bulk solution. ZIF-7 is an interesting filler material not only due to its use in selective light gas separations but also for its three different crystal phases. Herein, we carried out systematic investigations on the *in situ* confined formation of ZIF-7 phases inside a polymer (6FDA-DAM) by PMMOF. The reaction conditions of ZIF-7 in the polymer free volume were deduced based on a bulk-phase ZIF-7 phase diagram constructed by varying the ZIF-7 precursor concentrations and ratios. Based on the understanding of the reaction conditions, the ZIF-7 crystal phases formed inside the polymer during the PMMOF process were controlled, yielding 6FDA-DAM/ZIF-7 MMMs with three different crystal phases. The ZIF-7 phases had significant effects on the gas transport of MMMs with layered ZIF-7-III fillers exhibiting the highest performance enhancement for H_2/CO_2 separation (*i.e.*, H_2 permeability of ~1630 Barrer and H_2/CO_2 selectivity of ~3.8) among other phases. Furthermore, the MMMs obtained by the PMMOF process showed enhanced H_2/CO_2 separation performance, surpassing the upper bound.

Introduction

Metal–organic frameworks (MOFs) consist of metal nodes ligated by organic bridging ligands with the unique features of uniform pore structures, large surface areas, chemical and thermal stability, and tunable properties.[1,2] Due to these unique features, MOFs have attracted extensive attention for diverse applications including drug delivery, optics, catalysis, and gas separation.[3–6] In particular, the well-defined molecular scale pores and the tunable properties of MOFs make them ideal membrane materials for gas separations.[7] Of particular interest is their potential as functional fillers in mixed-matrix membranes (MMMs), which can overcome the limitations of polymeric membranes by taking advantage of both polymers and molecular sieving fillers.[8] Despite their promise and success in the literature,[9] MMMs have never been commercialized for industrial-scale applications. This is primarily due to the several challenging issues in the conventional blending-based MMM fabrication methods, including poor interfacial adhesion between MOFs and polymers, agglomeration of MOF fillers, limited filler loadings, and difficulty in forming MOF nanoparticles (smaller than 100 nm).[10] Even after addressing the above-mentioned issues, the conventional blending-based methods are hardly scalable since it is tremendously challenging to spin dope solutions containing fillers into commercially viable hollow fibers with sub-micron-thick selective skin composite layers.[8,11]

Recently, we developed and reported polymer-modification-enabled *in situ* metal–organic framework formation (PMMOF).[12] PMMOF enables MOF nanoparticles to form *in situ* inside polymers, effectively suppressing several issues faced by the conventional blending-based MMMs. Moreover, since PMMOF decouples the filler incorporation step and the MMM fabrication step, PMMOF is expected to be applied directly to large-scale commercially available polymer membranes, thereby enabling a simple upgrade of relatively cheap polymer membranes to more valuable MMMs. The properties of MMMs are greatly influenced by the microstructures (*i.e.*, phase, size, shape, *etc.*) of fillers, which often affect the microstructures of

---

[a] *Artie McFerrin Department of Chemical Engineering, Texas A&M University, 3122 TAMU, College Station, TX 77843-3122, USA. E-mail: hjeong7@tamu.edu*

[b] *Department of Industrial Chemistry, Pukyong National University, 45 Yongso-ro, Nam-gu, Busan 48513, Republic of Korea*

[c] *Department of Materials Science and Engineering, Texas A&M University, 3122 TAMU, College Station, TX 77843-3122, USA*

† Electronic supplementary information (ESI) available. See DOI: 10.1039/d0ta02761h

‡ These authors contributed equally to this work.

composites (*i.e.*, interface, distribution of fillers, *etc.*). Filler microstructures are determined by the synthesis reaction conditions (*e.g.*, precursor concentration, precursor diffusion, and chemical interactions).[13,14] Since the actual conditions for *in situ* MOF formation by PMMOF are expected to be quite different from those for MOF synthesis in a bulk solution, investigations on the actual synthesis conditions are very important yet quite challenging because of the nature of *in situ* synthesis in confined spaces.

Zeolitic-imidazole framework-7 (ZIF-7, Zn(bIm)$_2$) consists of zinc tetrahedrally coordinated with benzimidazole forming six-membered rings with a sodalite (SOD) topology.[2] ZIF-7 has been considered as one of the most important ZIFs reported, because of its unique gate-opening phenomenon, intrinsic thermal stability and hydrophobic properties, and excellent molecular sieving effects for mostly hydrogen over other light gases.[2,15,16] Moreover, ZIF-7 undergoes phase transformation with three different crystal phases:[17] a symmetric structure with a large-pore structure (ZIF-7-I, Phase I), a distorted structure of Phase I with a narrow-pore structure (ZIF-7-II, Phase II), which is transformed from Phase I when guest molecules such as DMF, water, and CO_2 are removed, and a layered structure with a nonporous structure (ZIF-7-III, Phase III), which is induced by the hydrolysis of Phase I or II. While the transformation between Phases I and II is reversible, the transformation of Phase I or II to Phase III is irreversible. It is noteworthy to mention that the formation of the three crystal phases of ZIF-7 is governed by synthesis parameters including precursor concentration, solvents, and post-treatments.[18] As such, the aforementioned unique features of ZIF-7 give a unique opportunity to investigate how the actual reaction conditions in PMMOF differ from those in solution precipitation.

There are a few reports on ZIF-7-based MMMs prepared by a conventional physical blending method. Li *et al.*[19] prepared poly(ether-*block*-amide)-1657 (Pebax®1657)/ZIF-7 MMMs and showed their promising separation performances for CO_2/N_2 and CO_2/CH_4 mixtures despite a decrease in CO_2 permeation. Also, Yang *et al.*[20] successfully incorporated ZIF-7 nanoparticles of <50 nm in size in polybenzimidazole (PBI) to up to 50 wt%. The resulting MMMs showed considerable performance improvement in H_2/CO_2 separation at temperatures up to 180 °C. They attributed the significantly enhanced H_2 permeability to the enlarged polymer free volume as ZIF-7 loading increased. Recently, enhanced gas separations were observed in MMMs with functionalized ZIF-7.[21,22]

Herein, we take systematic approaches to understand the *in situ* growth of ZIF-7 inside a polymer thin-film by PMMOF. 6FDA-DAM/ZIF-7 MMMs are fabricated by PMMOF and the crystal phase of the *in situ* formed ZIF-7 is compared with that of the ZIF-7 precipitated in a bulk solution. A crystal phase diagram for solution-precipitated ZIF-7 is constructed by varying important synthesis parameters in solutions. Based on the ZIF-7 phase diagram, the reaction condition of each ZIF-7 crystal phase is determined during PMMOF, which eventually leads to the formation of 6FDA-DAM/ZIF-7 MMMs with three different ZIF-7 crystal phases. Lastly, the gas separation properties of the resulting MMMs are examined under both single and mixed gas conditions to investigate the tunable gas separation performances of MMMs with different ZIF-7 crystal phases.

Experimental

Materials

6FDA-DAM (M_w: 148 kDa, PDI: 2.14) was purchased from Akron Polymer Systems Inc. Sodium formate (HCOONa, ≥99%, Sigma Aldrich), zinc nitrate hexahydrate ($Zn(NO_3)_2 \cdot 6H_2O$, 98%, Sigma Aldrich), and benzimidazole (HbIm) ($C_7H_6N_2$, ≥98%, Sigma Aldrich) were used for ZIF-7 synthesis. Ethanol (C_2H_5OH, 94–96%, Alfa Aesar) and *N*,*N*-dimethylformamide (DMF) (C_3H_7NO, >99.8%, Alfa Aesar) were used as solvents. Methanol (CH_3OH, >99.8%, Alfa Aesar) was used for washing. All chemicals were used as received.

ZIF-7 particle synthesis

A crystal phase diagram of ZIF-7 was constructed based on the solvothermal synthesis of ZIF-7 particles in a bulk solution. Both metal and linker precursor solutions were prepared by varying precursor compositions ranging between 0.1–100 mmol of zinc nitrate hexahydrate and 0.1–75 mmol of benzimidazole in ethanol/DMF co-solvents (30 ml, 99/1 v/v). A metal and a linker solution were mixed, and the precursor mixture solution was placed in a Teflon-lined stainless-steel autoclave. The synthesis was carried out at 100 °C for 2 h without stirring. The resulting ZIF-7 powder was decanted after centrifugation with 8000 rpm for 20 min. The powder sample was then purified by re-dispersing in methanol under sonication followed by centrifugation. This purification step was repeated two more times. The acquired ZIF-7 powder was dried at 60 °C overnight before characterizations.

Fabrications of 6FDA-DAM/ZIF-7 MMMs by PMMOF

A 2 wt% 6FDA-DAM solution in DMF was prepared as the stock polymer solution and used for polymer thin films on porous α-alumina substrates. Then, 2.4 ml of the polymer solution was slowly dropped onto the polished side of a home-made α-alumina disk. Porous α-alumina disks (22 mm in diameter, 2 mm in thickness, and 46% porosity with an average pore diameter of ∼200 nm) were prepared by following a previously reported recipe.[23] Thereafter, the sample was immediately placed into a vacuum oven and then dried at 150 °C for 24 h under vacuum. For hydrolysis, the 6FDF-DAM-coated α-alumina disk was vertically loaded on a custom-made Teflon holder and placed in a Teflon-lined autoclave containing a sodium formate solution (100 mmol of sodium formate in 30 ml of D.I. water). The hydrolysis reaction was performed at 120 °C for 5 h, followed by natural cooling to room temperature. The hydrolyzed polymer thin film was then washed with D.I. water overnight using a lab shaker to remove physically absorbed sodium and formate ions. A Zn ion exchange step was carried out by immersing the hydrolyzed polymer film into an ion-exchange solution (10, 25, or 50 mmol of zinc nitrate hexahydrate in 30 ml of D.I. water) at room temperature for 3 h followed by a simple rinsing with ethanol. The ligand treatment was performed by immersing the Zn ion-adsorbed film into a benzimidazole solution (25 mmol of HbIm in 30 ml of ethanol/DMF, 99/1 v/v) in a Teflon-lined autoclave at 100 °C for 2 h without stirring. After slow cooling the reactor to room temperature, the resulting film was washed with methanol overnight. Lastly, the imidization reaction was conducted by heating at 220 °C for 3 h in a pre-heated convection oven.

Characterizations

Scanning electron microscope (SEM) measurements were conducted using a JEOL JSM-7500F at an acceleration voltage of 5 keV with 15 mm working distance. Transmission electron microscope (TEM, JEOL JEM-2010) was operated at a voltage of 200 keV. X-ray diffraction (XRD, Rigaku Miniflex II) was performed in the 2θ range of 5°–40° with Cu-Kα radiation ($\lambda = 1.5406$ Å). Fourier transform infrared spectra (FT-IR) were taken using a Nicolet iS5 spectrometer (Thermo Scientific) equipped with attenuated total reflectance (ATR, iD7) accessory. X-ray photoelectron spectroscopy (XPS) measurements were conducted by an Omicron ESCA+ with Mg X-ray source at 300 W. Thermogravimetric analyses (TGA, Q50 TA instruments) were carried out under air over the temperature range of 25–800 °C with a heating rate of 10 °C min^{-1}.

Gas permeation measurements

Gas permeation tests were performed using the Wicke–Kallenbach technique at room temperature under atmospheric pressure. For single gases of H_2, CO_2, N_2, and CH_4, a feed gas was provided at 20 cm^3 min^{-1} while the permeate side was swept by argon gas with the flow rate of 20 cm^3 min^{-1}. Similarly, for equal-molar binary gas mixtures of H_2/CO_2, H_2/CH_4, and CO_2/N_2, the total feed flow rate was kept at 20 ml min^{-1}. The composition of the permeated gases was determined using a gas analyzer (QGA, Hiden Analytical).

Results and discussion

Fabrication and characterization of PI/ZIF-7 MMMs by PMMOF

6FDA-DAM/ZIF-7 MMMs were fabricated using our polymer-modification-enabled *in situ* metal–organic framework formation (PMMOF) process reported recently.[24] A 6FDA-DAM polyimide (PI) (Fig. S1a†) thin film was prepared on an α-alumina disk by a drop-casting method, resulting in a PI film with a thickness of 7.9 ± 2.0 μm. As shown in Fig. S1,† ZIF-7 was *in situ* formed inside the PI thin film by PMMOF, which consisted of four steps: hydrolysis, ion-exchange, ligand treatment, and imidization, each of which was monitored by ATR-FT-IR spectra (Fig. S2†). Detailed explanations are presented in ESI (Fig. S2 and S3†). The XRD patterns of the PI/ZIF-7 MMM matched with the simulated pattern of ZIF-7-I, which has a symmetric large-pore structure (Fig. 1a).[17] The cross-sectional SEM image of the PI/ZIF-7-I exhibited a grainy surface, which may or may not be ZIF-7, compared with the relatively smooth cross-section of the PI (Fig. 1b and c). Also, relatively large clusters were found on the top surface of the PI/ZIF-7-I (Fig. 1b). To confirm the presence of ZIF-7-I inside the PI, the surface of the PI/ZIF-7-I was gently wiped using a diluted nitric acid solution (0.1 M). Since ZIFs are very sensitive to acid,[25] the acid treatment removed most of the clusters present on the top surface of the PI/ZIF-7-I (Fig. S4†). In addition, some of the ZIF-7-I formed in the vicinity of the external surface appeared to be partially removed as well (see the red dashed area in Fig. S4†). The XRD patterns of the PI/ZIF-7-I after acid treatment showed slightly reduced peak intensities relative to that of the pattern before acid treatment (Fig. S5†), suggesting that a majority of the ZIF-7-I were formed inside the polymer. The cross-sectional TEM image of the sample in the inset of Fig. 1b shows poorly defined ZIF-7-I crystals of less than 100 nm in size. Based on these observations, it was concluded that ZIF-7-I nanoparticles less than 100 nm in size were formed mostly inside the PI film by PMMOF.

In the PMMOF process, crystallization happens in confined spaces inside the polymer (*i.e.*, free volumes),[24,26] thereby affecting the diffusion of precursor species inside the polymer film as well as interactions of reacting species. In other words, ZIF-7 crystallization inside a PAA-Zn film proceeds in a different environment than in a bulk solution. To confirm this, ZIF-7 was synthesized in a solution under the same reaction condition as the PMMOF process. The obtained ZIF-7 powders exhibited the ZIF-7-III (dense layered structure) phase and were several microns in size (Fig. S6†). The formation of a different ZIF-7 crystal phase in the bulk solution *vs.* that in PMMOF strongly suggests that the actual reaction conditions are very different.

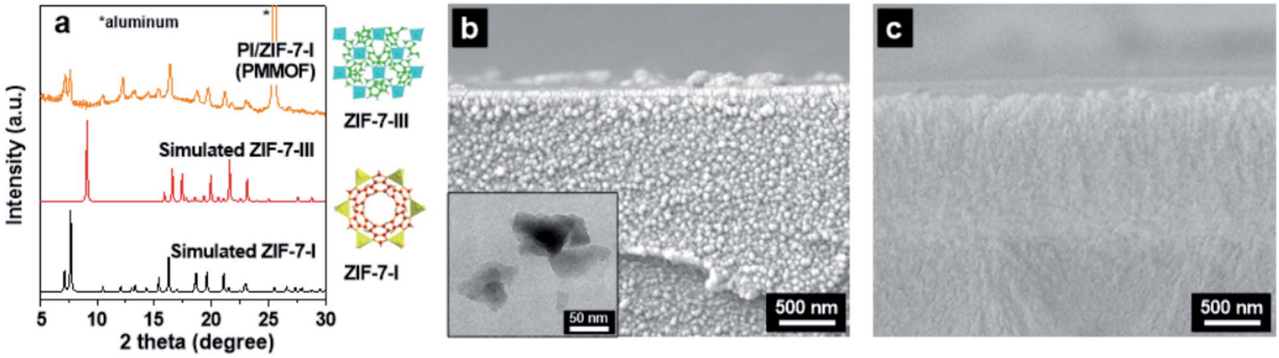

Fig. 1 (a) XRD patterns and (b) cross-sectional SEM images of as-prepared PI/ZIF-7-I by PMMOF. The inset in (b) is the TEM image of *in situ* formed ZIF-7-I in the polymer. (c) Cross-sectional SEM image of the PI that was hydrolysed and then imidized.

On the other hand, the much smaller particles of *in situ* grown ZIF-7 (lp) by PMMOF can be attributed mainly to the unique confined environments inside the polymer. It was, therefore, hypothesized that the concentrations and ratios of both absorbed Zn and bIm precursors inside the polymer film can be important parameters to determine the ZIF-7 crystal phase.

ZIF-7 crystal phase diagram and PMMOF reaction conditions

To confirm our hypothesis on the effect of precursor concentrations and ratios inside the polymer film on ZIF-7 crystal phase, a ZIF-7 crystal phase diagram was established by varying the concentrations and ratios of Zn ions and bIm ligands using bulk solution reaction. The acquired ZIF-7 particles were characterized by SEM and XRD to investigate their crystal phases (Fig. S7 and S8†). Four distinctive regions were identified in the crystal phase diagram (see Fig. 2a): (1) ZIF-7-I phase (marked with red spots), (2) ZIF-7-mix mixed-phase containing both ZIF-7-I and ZIF-7-III phases (marked with yellow spots), (3) ZIF-7-III phase (marked with green spots), and (4) undefinable region due to the lack of precipitations (marked with a dashed line). The representative SEM images and XRD patterns for the three distinctive ZIF-7-I, ZIF-7-mix, and ZIF-7-III samples collected from bulk solutions are displayed in Fig. S7 and S8,† respectively. The SEM images presented a spherical shape for ZIF-7-I with sub-micron size and a planar shape for ZIF-7-mix and ZIF-7-III with micron size (Fig. S7†). ZIF-7-III showed a smooth surface. In the case of ZIF-7-mix, however, ZIF-7-III seemed covered with the debris of ZIF-7-I, suggesting that the two different crystal phases including ZIF-7-I and ZIF-7-III were seemingly physically mixed (Fig. S7†).

Based on the ZIF-7 crystal phase diagram, the reaction conditions of the *in situ* synthesis of ZIF-7 in the polymer by PMMOF were evaluated by tracking precursor concentrations at three stages: (1) when a PAA film was immersed in the zinc solution, (2) when the polymer film was saturated with Zn ions, (3) when a PAA/ZIF-7 was formed after ligand treatment. The concentration of Zn ions was determined by the amount of evaporated solvents and zinc oxide residues formed by thermal oxidization of dried samples (Fig. S9†). It is noted that the determined amounts of zinc sources are based on mobile Zn ions rather than immobile Zn ions coordinated to the polymer (confirmed by the XPS analysis in Fig. S10†). This is because the mobile zinc sources mainly contribute to form ZIF inside the polymer.[12,26] Initially, as indicated at the point (1) in Fig. 2a, the concentration of Zn ions in the mother solution was 0.42 mol kg^{-1}. By immersing a PAA film in the zinc solution, Zn ions were absorbed into the polymer free volume (Fig. 2b(1)). When the polymer was fully saturated with the Zn ions, as shown in Fig. 2b(2), the total concentration of Zn ions in the PAA film was 1.51 ± 0.08 mol kg^{-1}, and the concentration of mobile Zn ions was 0.89 ± 0.05 mol kg^{-1} (see the point (2) in Fig. 2a). The Zn ion concentration in the polymer (*i.e.*, 0.89 ± 0.05 mol kg^{-1}) was two times higher than that in the mother solution (*i.e.*, 0.42 mol kg^{-1}). This relatively high zinc concentration inside the PAA film can be explained by the fact that Zn ions were thermodynamically preferred inside the film while solvent molecules were preferred in the solution, probably due to (1) the electrostatic interaction of Zn ions with the charged polymer and (2) the much smaller size of Zn ions as compared to ethanol (*i.e.*, 0.74 Å of zinc ionic radius *vs.* 4.5 Å of ethanol critical diameter).[27] After ligand treatment using the bIm solution with bIm concentration of 1.05 mol kg^{-1}, the concentration of mobile Zn ions was reduced to 0.053 ± 0.012 mol kg^{-1} (see the point (3) in Fig. 2a). As depicted in Fig. 2b(3), a majority of Zn ions were drained from the PAA free volume and bIm ligands were absorbed into the polymer upon ligand treatment possibly due to the applied electric potential gradient of the precursors inside and outside the polymer.[28] The remaining Zn ions inside the polymer free volume were simultaneously reacted with the absorbed bIm ions upon solvothermal ligand treatment, resulting in the nucleation and growth of ZIF-7 nanocrystals in the PAA free volume (Fig. 2b(3)). At the final mobile Zn ion concentration (*i.e.*, 0.053 ± 0.012 mol kg^{-1}), it was found that the ZIF-7-I phases were presented in the very narrow bIm concentrations ranging from 0.65 mol kg^{-1} to 1.05 mol kg^{-1} in the ZIF-7 phase diagram (Fig. 2a). Since the PI/ZIF-7 by PMMOF exhibited the ZIF-7-I phase (Fig. 1a), the synthesis conditions (*i.e.*, concentrations of Zn ions and bIm ligands) for ZIF-7 by PMMOF was estimated in region (3) in Fig. 2a.

Engineering of ZIF-7 crystal phase of PI/ZIF-7 MMM

The performances of ZIF-7-containing MMMs are expected to be greatly affected by the ZIF-7 phase *in situ* formed by PMMOF. As such, we attempted to test if the ZIF-7 phase diagram and the

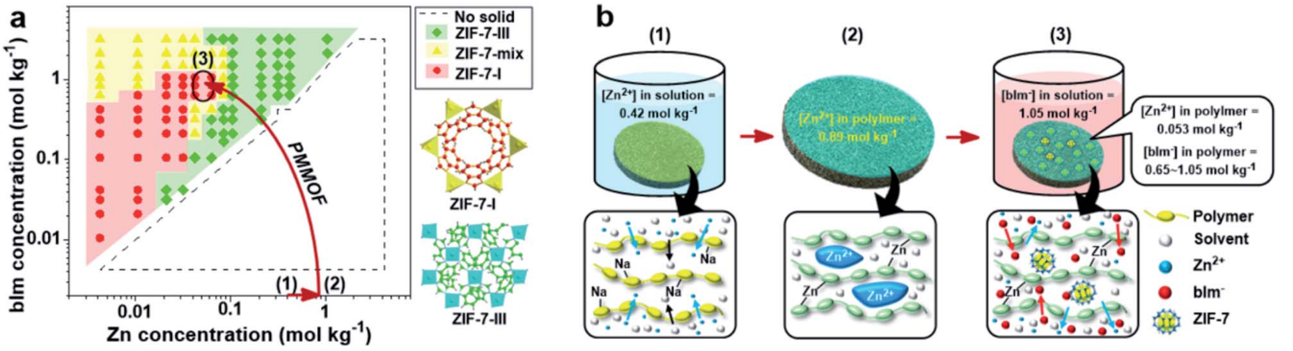

Fig. 2 (a) ZIF-7 crystal phase diagram as a function of concentrations of zinc and bIm. (b) Illustration of the ZIF-7 synthesis stages and the corresponding conditions upon PMMOF process.

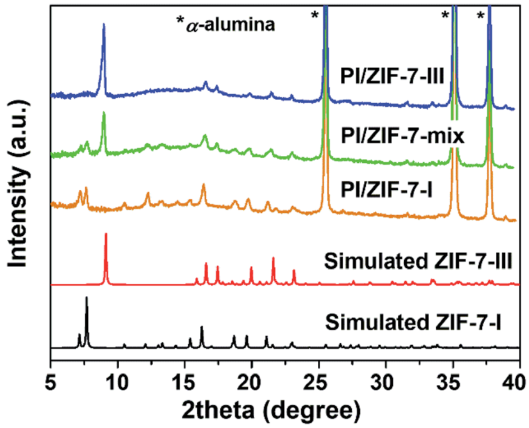

Fig. 3 XRD patterns of PI/ZIF-7 MMMs by PMMOF with three different ZIF-7 crystal phases.

evaluated PMMOF reaction conditions can be used to control the formation of not only ZIF-7-I but also the other phases (*i.e.*, ZIF-7-mix and ZIF-7-III). As discussed above, PI/ZIF-7-I MMMs were formed when the zinc concentration in a mother solution was 0.42 mol kg^{-1} (see the α region in Fig. S11†). As the zinc concentration in an ion exchange solution increased to 1.05 mol kg^{-1}, the ZIF-7-mix mixed-phase was acquired (see the β region in Fig. S11†) with the crystal phase composition of ZIF-7-I (51%) and ZIF-7-III (49%) (Fig. 3). It is noted that the percentages of each ZIF-7 phase were calculated by integrating the intensive XRD peaks of (101) and (110) for ZIF-7-I and (002) for ZIF-7-III. When the zinc concentration in an ion exchange solution further increased to 2.11 mol kg^{-1}, the ZIF-7-III phase was formed (see the γ region in Fig. S11†), confirmed by the absence of (101) and (110) peaks in the XRD pattern (Fig. 3). The ZIF-7 phases present in MMMs by PMMOF well corresponded to those estimated in the phase diagram. This indicates that the phase diagram and the estimated reaction conditions inside the polymer free volume can give a reasonable guideline to control the ZIF-7 phase in PI/ZIF-7 MMMs by PMMOF.

Interestingly, both PI/ZIF-7-mix and PI/ZIF-7-III MMMs exhibited an almost identical cross-sectional morphology as PI/ZIF-7-I (Fig. S12†). Regardless of the crystal phase, the size of the *in situ* grown ZIF-7 nanoparticles seemed to be significantly smaller than those of the crystals synthesized by the solution reaction (*i.e.*, >1 μm) (Fig. S7†). The suppression of micro-sized particle formation was attributed to the confined growth inside the polymer (*i.e.*, free volume). It is highly desirable to have nano-sized fillers for ultra-thin MMM layers, in particular, asymmetric mixed-matrix hollow fiber membranes.[11] In addition, it was found that total ZIF-7 loading in MMMs could increase with changing ZIF-7 phases from ZIF-7-I to ZIF-7-III (Table S1†). The ZIF-7 loadings in PI/ZIF-7 MMMs by PMMOF were determined using TGA analysis, which is described in detail in ESI (Table S1†). The ZIF-7-I content in a PI/ZIF-7-I MMM was estimated at 2.78 wt%. With an increase in Zn

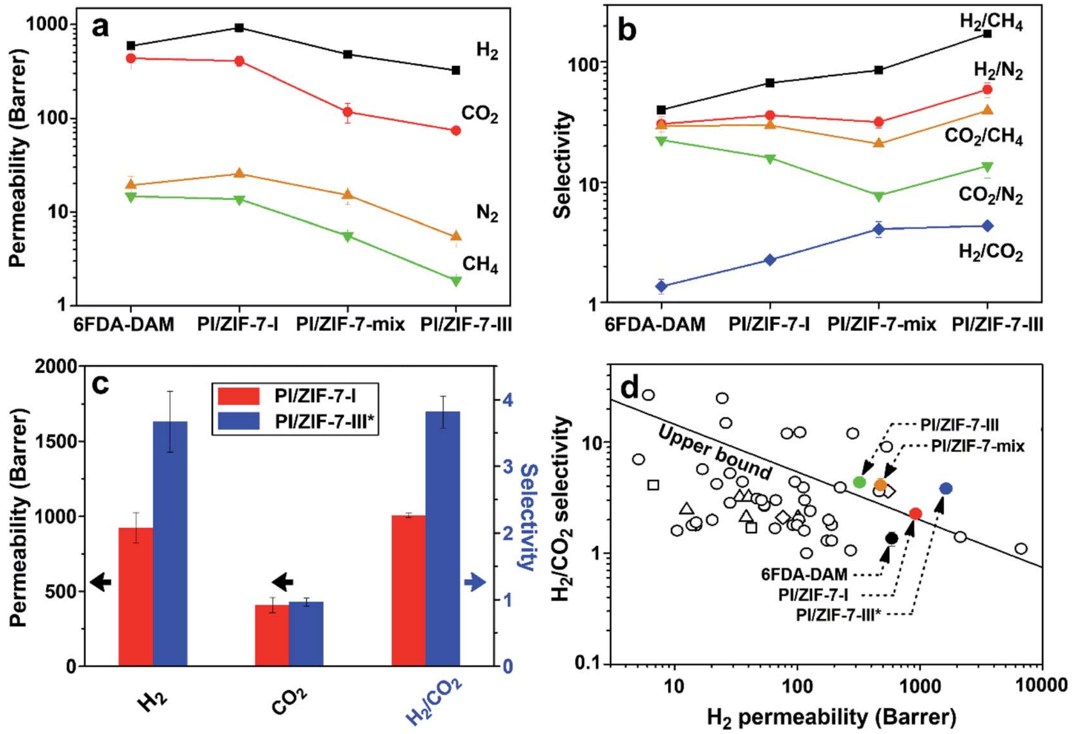

Fig. 4 Single gas transport results of PI/ZIF-7 MMMs by PMMOF at room temperature under atmospheric pressure. (a) Permeability, (b) selectivity of 6FDA-DAM, PI/ZIF-7-I (~3 wt%), PI/ZIF-7-mix (~7 wt%), and PI/ZIF-7-III (~10 wt%), (c) comparison of H_2/CO_2 separation properties of PI/ZIF-7-I (~3 wt%) and PI/ZIF-7-III* (~3 wt%), and (d) H_2/CO_2 separation performance of PI/ZIF-7 MMMs by PMMOF (●) in comparison with those of the MOF-based (○), zeolite-based (△), carbon-based (□), and silica-based (◇) MMMs reported.[20,36–73]

concentration relative to that for PI/ZIF-7-I, 7.00 wt% for ZIF-7-mix in PI/ZIF-7-mix and 9.96 wt% for ZIF-7-III in PI/ZIF-7-III were formed (Table S1†).

Gas transport properties of PI/ZIF-7 MMMs by PMMOF

The single gas permeation of a pristine 6FDA-DAM polymer membrane exhibited similar properties to the reported results for H_2, CO_2, N_2, and CH_4 (Fig. 4 and Table S2†).[29,30] When compared with pristine 6FDA-DAM polymers, the PI/ZIF-7-I MMMs by PMMOF showed increased permeabilities for non-condensable gases (*i.e.*, H_2 and N_2) and decreased permeabilities for condensable gas molecules (*i.e.*, CO_2 and CH_4) (Fig. 4a and Table S2†). This result can be ascribed to the presence of microporous ZIF-7-I which allows a fast diffusion of non-condensable gases and a retarded diffusion of condensable gases *via* relatively strong sorption.[31,32] The ideal selectivities of H_2/CO_2, H_2/N_2, and H_2/CH_4 pairs of MMMs increased from 1.36, 30.62, and 40.23 to 2.26, 36.12, and 67.42, respectively. In contrast, there was a slight decrease in the ideal selectivity of CO_2/N_2 (22.54 → 15.97) (Fig. 4b). The increased ideal selectivities of H_2/CO_2, H_2/N_2, and H_2/CH_4 pairs are likely due to the molecular sieving effect of ZIF-7-I, whose crystallographically defined aperture size is ~3.0 Å,[33] given the kinetic diameter of hydrogen (2.89 Å). Since the kinetic diameters of both CO_2 and N_2 are 3.3 Å and 3.64 Å, respectively, both molecules can be excluded by ZIF-7-I (Fig. 4b). As such, the decreased CO_2/N_2 selectivity can be primarily due to the fact that CO_2 and N_2 interact with ZIF-7-I differently (*i.e.*, CO_2 interacts more strongly than N_2). Moreover, as compared with the single gas separation, the mixed gas separation factors were depressed except for H_2/CH_4, likely due to the competition between two different gas molecules (Fig. S13†).[34] Further explanation is in ESI (Fig. S13†).

As discussed above, ZIF-7 loading increased in the following order: PI/ZIF-7-I < PI/ZIF-7-mix < PI/ZIF-7-III (Table S1†). Nevertheless, the gas permeabilities increased in the opposite order for all gases tested: PI/ZIF-7-I > PI/ZIF-7-mix > PI/ZIF-7-III (Fig. 4a). This decreasing trend of gas permeability with an increase in ZIF-7 filler loading can be most likely due to the presence of the less permeable ZIF-7-III phase in MMMs (*i.e.*, ZIF-7-III works as a gas barrier).[17] Nevertheless, the ideal gas selectivities of the PI/ZIF-7-III except for CO_2/N_2 were higher than those of the ZIF-7-I MMM (Fig. 4b). This can be explained to be because the ZIF-7-III nanoparticles *in situ* grown in the polymer free volume might be loosely stacked, thereby showing a possible molecular sieving effect of ZIF-7-III. Furthermore, the polymer matrices in PI/ZIF-7 MMMs might become less permeable as ZIF-7 loadings increase since ZIF-7 crystals are formed in the polymer free volumes, resulting in the reduction of PI free volume.[12]

Since the filler content has a great effect on the gas transport properties of MMMs, it is important to compare the transport properties of MMMs with the same filler content in order to discern the effects of fillers. Due to the nature of PMMOF, it is, however, not straight forward to fabricate PI/ZIF-7 MMMs made of three different ZIF-7 phases with the same filler contents. To examine the filler effects, PI/ZIF-7-III MMMs were prepared by a post-phase-transformation from ZIF-7-I-containing MMMs using the hydrolysis process in water at 150 °C for 3 h. Initially, we attempted to perform hydrolysis on PI/ZIF-7-I. Unfortunately, 6FDA-DAM is hydrophobic, impeding sufficient water adsorption in MMMs, so it resulted in incomplete hydrolysis regardless of the reaction time.[29] Meanwhile, PAA/ZIF-7-I was relatively more hydrophilic, where PAA (*i.e.*, poly(amic acid)) is deimidized PI, which resulted in complete hydrolysis, leading to the transformation of ZIF-7-I to ZIF-7-III in the polymer. This phase transformation was confirmed by XRD (Fig. S14†).[30] PAA/ZIF-7-III was then imidized to obtain PI/ZIF-7-III, which is denoted as PI/ZIF-7-III* to distinguish it from PI/ZIF-7-III, whose ZIF-7-III is *in situ* formed *via* PMMOF.

The gas permeation properties of PI/ZIF-7-III* MMMs were tested and compared with those of PI/ZIF-7-I. As presented in Fig. 4c, PI/ZIF-7-III* MMMs showed higher H_2 permeability with similar CO_2 permeability, which is ascribed to the intrinsic property of ZIF-7-III. Peng *et al.*[35] showed that disorderly stacked exfoliated ZIF-7-III nanosheets showed an exceptionally high H_2/CO_2 separation performance. They claimed that the four-membered rings of the ZIF-7-III nanosheets consisting of flexible organic linkers allowed high H_2 permeation while excluding larger CO_2.[35] Hence, PI/ZIF-7-III* showed greater H_2/CO_2 selectivity by ~70% than PI/ZIF-7-I, which can be attributed to the better molecular sieving effect of ZIF-7-III than that of ZIF-7-I for H_2/CO_2 separation.[33,35]

When compared with other reported MMMs, the PI/ZIF-7 MMMs by PMMOF showed high H_2 permeability and H_2/CO_2 ideal selectivity, effectively surpassing the polymeric upper bound (Fig. 4d).[20,36–73] While most of the reported MMMs showed mediocre H_2/CO_2 ideal selectivity improvement from their corresponding pristine polymers, the PI/ZIF-7 MMMs by PMMOF exhibited up to ~220% enhancement in the H_2/CO_2 ideal selectivity (Table S3†). These enhancements are quite surprising considering the relatively low filler loadings (*i.e.*, ~10 wt%), indicating the exceptionally high filler efficiency (Table S3†). In particular, the PBI/ZIF-7 MMMs prepared by the conventional physical blending method, even with 50 wt% ZIF-7-I loading, showed an improvement in the H_2/CO_2 ideal selectivity from 8.7 to 14.9 (~70% improvement).[20] On the contrary, the PI/ZIF-7 MMMs by PMMOF with 2.78 wt% ZIF-7 loadings exhibited ~66% and ~180% improvement for ZIF-7-I and ZIF-7-III*, respectively, (Table S3†). However, the separation performance of other gas pairs rarely exceeded the corresponding upper bounds (Fig. S14†).

Conclusions

In conclusion, we prepared 6FDA-DAM/ZIF-7 MMMs using PMMOF by *in situ* growing ZIF-7 nanoparticles inside the polymer. To understand the different synthesis conditions between confined and bulk synthesis, a ZIF-7 phase diagram was constructed based on bulk solution synthesis. The ZIF-7 phase diagram was utilized to estimate and design 6FDA-DAM/ZIF-7 MMMs by PMMOF, resulting in the controlled synthesis of three different ZIF-7 phases (*i.e.*, ZIF-7-I, ZIF-7-mix, and ZIF-7-III). Among the MMMs, the ZIF-7-III*-based MMMs where

ZIF-7-III* was transformed from ZIF-7-I, even with 2.78 wt% filler loading, showed the best H_2/CO_2 separation performances, exhibiting dramatic improvements. The PI/ZIF-7-III* MMMs exhibited improved H_2 permeability and enhanced H_2/CO_2 selectivity by ~176% and ~180%, respectively, as compared with 6FDA-DAM and by ~77% and ~69%, respectively, as compared with PI/ZIF-7-I with the same filler loading. This enhancement was likely due to the more efficient molecular sieving property of ZIF-7-III than that of ZIF-7-I. The current findings are expected to be an important stepping stone for the further development of the PMMOF process for *in situ* formed MOF-based MMMs and scalable MMMs.

Conflicts of interest

There are no conflicts to declare.

Acknowledgements

H.-K. J. acknowledges the financial support from the National Science Foundation (CBET-1510530 and CBET-1929596). This publication was made possible in part by NPRP grant # 8-001-2-001 from the Qatar National Research Fund (a member of Qatar Foundation). The findings achieved herein are solely the responsibility of the authors. The National Science Foundation supported the FE-SEM acquisition under Grant DBI-0116835, the VP for Research Office, and the Texas A&M Engineering Experimental Station. We would like to thank Dr Micah Green and Mr Xiaofei Zhao for the help to use TGA.

Notes and references

1 H. Li, M. Eddaoudi, M. O'Keeffe and O. M. Yaghi, *Nature*, 1999, **402**, 276–279.
2 K. S. Park, Z. Ni, A. P. Cote, J. Y. Choi, R. D. Huang, F. J. Uribe-Romo, H. K. Chae, M. O'Keeffe and O. M. Yaghi, *Proc. Natl. Acad. Sci. U. S. A.*, 2006, **103**, 10186–10191.
3 M.-X. Wu and Y.-W. Yang, *Adv. Mater.*, 2017, **29**, 1606134.
4 Y. J. Cui, Y. F. Yue, G. D. Qian and B. L. Chen, *Chem. Rev.*, 2012, **112**, 1126–1162.
5 M. Yoon, R. Srirambalaji and K. Kim, *Chem. Rev.*, 2012, **112**, 1196–1231.
6 J. R. Li, J. Sculley and H. C. Zhou, *Chem. Rev.*, 2012, **112**, 869–932.
7 J. R. Li, R. J. Kuppler and H. C. Zhou, *Chem. Soc. Rev.*, 2009, **38**, 1477–1504.
8 M. R. A. Hamid and H. K. Jeong, *Korean J. Chem. Eng.*, 2018, **35**, 1577–1600.
9 B. Zornoza, C. Tellez, J. Coronas, J. Gascon and F. Kapteijn, *Microporous Mesoporous Mater.*, 2013, **166**, 67–78.
10 H. B. T. Jeazet, C. Staudt and C. Janiak, *Dalton Trans.*, 2012, **41**, 14003–14027.
11 C. Zhang, K. Zhang, L. R. Xu, Y. Labreche, B. Kraftschik and W. J. Koros, *AIChE J.*, 2014, **60**, 2625–2635.
12 S. Park, M. R. Abdul Hamid and H.-K. Jeong, *ACS Appl. Mater. Interfaces*, 2019, **11**, 25949–25957.
13 A. Schejn, L. Balan, V. Falk, L. Aranda, G. Medjahdi and R. Schneider, *CrystEngComm*, 2014, **16**, 4493–4500.
14 J. Cravillon, R. Nayuk, S. Springer, A. Feldhoff, K. Huber and M. Wiebcke, *Chem. Mater.*, 2011, **23**, 2130–2141.
15 S. Aguado, G. Bergeret, M. P. Titus, V. Moizan, C. Nieto-Draghi, N. Bats and D. Farrusseng, *New J. Chem.*, 2011, **35**, 546–550.
16 Y. S. Li, F. Y. Liang, H. Bux, A. Feldhoff, W. S. Yang and J. Caro, *Angew. Chem., Int. Ed.*, 2010, **49**, 548–551.
17 P. Zhao, G. I. Lampronti, G. O. Lloyd, M. T. Wharmby, S. Facq, A. K. Cheetham and S. A. T. Redfern, *Chem. Mater.*, 2014, **26**, 1767–1769.
18 M. He, J. F. Yao, L. X. Li, K. Wang, F. Y. Chen and H. T. Wang, *ChemPlusChem*, 2013, **78**, 1222–1225.
19 T. Li, Y. C. Pan, K. V. Peinemann and Z. P. Lai, *J. Membr. Sci.*, 2013, **425**, 235–242.
20 T. X. Yang, Y. C. Xiao and T. S. Chung, *Energy Environ. Sci.*, 2011, **4**, 4171–4180.
21 L. Xiang, L. Q. Sheng, C. Q. Wang, L. X. Zhang, Y. C. Pan and Y. S. Li, *Adv. Mater.*, 2017, **29**, 1606999–1607006.
22 B. A. Al-Maythalony, A. M. Alloush, M. Faizan, H. Dafallah, M. A. A. Elgzoly, A. A. A. Seliman, A. Al-Ahmed, Z. H. Yamani, M. A. M. Habib, K. E. Cordova and O. M. Yaghi, *ACS Appl. Mater. Interfaces*, 2017, **9**, 33401–33407.
23 M. J. Lee, H. T. Kwon and H. K. Jeong, *Angew. Chem., Int. Ed.*, 2018, **57**, 156–161.
24 S. Park, M. R. A. Hamid and H. K. Jeong, *ACS Appl. Mater. Interfaces*, 2019, **11**, 25949–25957.
25 C. Han, C. Y. Zhang, N. Tyminska, J. R. Schmidt and D. S. Sholl, *J. Phys. Chem. C*, 2018, **122**, 4339–4348.
26 M. R. A. Hamid, S. Park, J. S. Kim, Y. M. Lee and H. K. Jeong, *J. Mater. Chem. A*, 2019, **7**, 9680–9689.
27 Z. Song, Y. Huang, W. L. Xu, L. Wang, Y. Bao, S. Li and M. Yu, *Sci. Rep.*, 2015, **5**, 13981.
28 S. Al-Amshawee, M. Y. B. Yunus, A. A. M. Azoddein, D. G. Hassell, I. H. Dakhil and H. Abu Hasan, *Chem. Eng. J.*, 2020, **380**, 2130–2134.
29 C. Zhang, R. P. Lively, K. Zhang, J. R. Johnson, O. Karvan and W. J. Koros, *J. Phys. Chem. Lett.*, 2012, **3**, 2130–2134.
30 Y. S. Do, W. H. Lee, J. G. Seong, J. S. Kim, H. H. Wang, C. M. Doherty, A. J. Hill and Y. M. Lee, *Chem. Commun.*, 2016, **52**, 13556–13559.
31 W. Morris, N. He, K. G. Ray, P. Klonowski, H. Furukawa, I. N. Daniels, Y. A. Houndonougbo, M. Asta, O. M. Yaghi and B. B. Laird, *J. Phys. Chem. C*, 2012, **116**, 24084–24090.
32 S. Park, E. Jang, H. An, W. Choi, J. H. Kim, J. H. Lee, J. Choi and J. S. Lee, *Microporous Mesoporous Mater.*, 2018, **264**, 60–69.
33 Y.-S. Li, F.-Y. Liang, H. Bux, A. Feldhoff, W.-S. Yang and J. Caro, *Angew. Chem., Int. Ed.*, 2010, **49**, 548–551.
34 S. Park, A. S. Lee, Y. S. Do, J. F. Kim, S. S. Hwang, Y. M. Lee, J. H. Lee and J. S. Lee, *J. Membr. Sci.*, 2016, **516**, 202–214.
35 Y. Peng, Y. Li, Y. Ban, H. Jin, W. Jiao, X. Liu and W. Yang, *Science*, 2014, **346**, 1356–1359.
36 E. V. Perez, K. J. Balkus, J. P. Ferraris and I. H. Musselman, *J. Membr. Sci.*, 2009, **328**, 165–173.

37 E. Karatay, H. Kalipcilar and L. Yilmaz, *J. Membr. Sci.*, 2010, **364**, 75–81.

38 B. Zornoza, O. Esekhile, W. J. Koros, C. Tellez and J. Coronas, *Sep. Purif. Technol.*, 2011, **77**, 137–145.

39 J. Ahmad and M. B. Hagg, *Sep. Purif. Technol.*, 2013, **115**, 190–197.

40 B. Seoane, C. Tellez, J. Coronas and C. Staudt, *Sep. Purif. Technol.*, 2013, **111**, 72–81.

41 S. N. Wijenayake, N. P. Panapitiya, S. H. Versteeg, C. N. Nguyen, S. Goel, K. J. Balkus, I. H. Musselman and J. P. Ferraris, *Ind. Eng. Chem. Res.*, 2013, **52**, 6991–7001.

42 M. Arjmandi and M. Pakizeh, *J. Ind. Eng. Chem.*, 2014, **20**, 3857–3868.

43 J. O. Hsieh, K. J. Balkus, J. P. Ferraris and I. H. Musselman, *Microporous Mesoporous Mater.*, 2014, **196**, 165–174.

44 G. L. Zhuang, H. H. Tseng and M. Y. Wey, *Int. J. Hydrogen Energy*, 2014, **39**, 17178–17190.

45 M. S. Boroglu and A. B. Yumru, *Sep. Purif. Technol.*, 2017, **173**, 269–279.

46 E. V. Perez, G. J. D. Kalaw, J. P. Ferraris, K. J. Balkus and I. H. Musselman, *J. Membr. Sci.*, 2017, **530**, 201–212.

47 Q. Z. Xue, X. L. Pan, X. F. Li, J. Q. Zhang and Q. K. Guo, *Nanotechnology*, 2017, **28**, 065702–065711.

48 M. Arjmandi, M. Pakizeh, M. Saghi and A. J. P. C. Arjmandi, *Pet. Chem.*, 2018, **58**, 317–329.

49 M. Lanč, P. Sysel, M. Šoltys, F. Štěpánek, K. Fónod, M. Klepić, O. Vopička, M. Lhotka, P. Ulbrich and K. Friess, *Polymer*, 2018, **144**, 33–42.

50 A. Pulyalina, G. Polotskaya, V. Rostovtseva, Z. Pientka and A. Toikka, *Polymer*, 2018, **10**, 828–839.

51 A. B. Yumru, M. Safak Boroglu and I. Boz, *Greenhouse Gases: Sci. Technol.*, 2018, **8**, 529–541.

52 L. M. Robeson, *J. Membr. Sci.*, 2008, **320**, 390–400.

53 D. Fritsch, K-V. Peinemann and D. D. F. Gomes, *US Pat.*, US7658784B2, 2010.

54 A. Car, C. Stropnik and K.-V. Peinemann, *Desalination*, 2006, **200**, 424–426.

55 Y. Zhang, I. H. Musselman, J. P. Ferraris and K. J. Balkus, *J. Membr. Sci.*, 2008, **313**, 170–181.

56 C. Liu, B. McCulloch, S. T. Wilson, A. I. Benin and M. E. Schott, *US Pat.*, US7637983B1, 2009.

57 E. V. Perez, K. J. Balkus, J. P. Ferraris and I. H. Musselman, *J. Membr. Sci.*, 2009, **328**, 165–173.

58 M. J. C. Ordoñez, K. J. Balkus, J. P. Ferraris and I. H. Musselman, *J. Membr. Sci.*, 2010, **361**, 28–37.

59 K. Díaz, M. López-González, L. F. del Castillo and E. Riande, *J. Membr. Sci.*, 2011, **383**, 206–213.

60 Q. Song, S. K. Nataraj, M. V. Roussenova, J. C. Tan, D. J. Hughes, W. Li, P. Bourgoin, M. A. Alam, A. K. Cheetham, S. A. Al-Muhtaseb and E. Sivaniah, *Energy Environ. Sci.*, 2012, **5**, 8359–8369.

61 T. Yang, G. M. Shi and T.-S. Chung, *J. Mater. Chem. A*, 2012, **2**, 1358–1367.

62 T. Yang and T.-S. Chung, *Int. J. Hydrogen Energy*, 2013, **38**, 229–239.

63 A. F. Bushell, M. P. Attfield, C. R. Mason, P. M. Budd, Y. Yampolskii, L. Starannikova, A. Rebrov, F. Bazzarelli, P. Bernardo, J. Carolus Jansen, M. Lanč, K. Friess, V. Shantarovich, V. Gustov and V. Isaeva, *J. Membr. Sci.*, 2013, **427**, 48–62.

64 T. Yang and T.-S. Chung, *J. Mater. Chem. A*, 2013, **1**, 6081–6090.

65 L. Ge, W. Zhou, V. Rudolph and Z. Zhu, *J. Mater. Chem. A*, 2013, **1**, 6350–6358.

66 B. Seoane, V. Sebastián, C. Téllez and J. Coronas, *CrystEngComm*, 2013, **15**, 9483–9490.

67 L. Cao, K. Tao, A. Huang, C. Kong and L. Chen, *Chem. Commun.*, 2013, **49**, 8513–8515.

68 S. Sorribas, B. Zornoza, C. Téllez and J. Coronas, *J. Membr. Sci.*, 2014, **452**, 184–192.

69 A. Bhaskar, R. Banerjee and U. Kharul, *J. Mater. Chem. A*, 2014, **2**, 12962–12967.

70 L. Li, J. Yao, X. Wang, Y.-B. Cheng and H. Wang, *J. Appl. Polym. Sci.*, 2014, **131**, 41056–41062.

71 D. Carter, F. H. Tezel, B. Kruczek and H. Kalipcilar, *J. Membr. Sci.*, 2017, **544**, 35–46.

72 J. Sánchez-Laínez, B. Zornoza, Á. Mayoral, Á. Berenguer-Murcia, D. Cazorla-Amorós, C. Téllez and J. Coronas, *J. Mater. Chem. A*, 2015, **3**, 6549–6556.

73 Z. Kang, Y. Peng, Z. Hu, Y. Qian, C. Chi, L. Y. Yeo, L. Tee and D. Zhao, *J. Mater. Chem. A*, 2015, **3**, 20801–20810.